Research Square

Preprints are preliminary reports that have not undergone peer review.
They should not be considered conclusive, used to inform clinical practice,
or referenced by the media as validated information.

Closed-loop AI enables time- and resource-efficient optimization of processing pathways without microstructural input

Sreenivas Raguraman

sreenivas.raguraman@mat.ethz.ch

ETH Zurich https://orcid.org/0000-0003-4899-7471

Maitreyee Sharma Priyadarshini

msharmap@vt.edu

Virginia Tech https://orcid.org/0000-0003-4950-2792

Andrew Kim

Johns Hopkins University

Tunde Ayodeji

Johns Hopkins University

Veronica Ivanovskaya

Johns Hopkins University

Camryn Byrum

Johns Hopkins University

Ryan McGovern

Johns Hopkins University

Adam J. Griebel

Fort Wayne Metals

Paulette Clancy

Johns Hopkins University

Timothy P. Weihs

Johns Hopkins University

Research Article

Keywords: Materials processing, Closed-loop optimization, Process-property relationships, Bayesian optimization, Machine learning, Biodegradable magnesium alloys

Posted Date: November 19th, 2026

DOI: https://doi.org/10.21203/rs.3.rs-11719391/v1

License: This work is licensed under a Creative Commons Attribution 4.0 International License.
Read Full License

Additional Declarations: The authors declare no competing interests.

Closed-loop AI enables time- and resource-efficient optimization of processing pathways without microstructural input

Sreenivas Raguraman[a,b,1,*], Maitreyee Sharma Priyadarshini[c,d,*], Andrew Kim[a], Tunde Ayodeji[e], Veronica Ivanovskaya[a], Camryn Byrum[f], Ryan McGovern[f], Adam J. Griebel[g], Paulette Clancy[c,a,b], Timothy P. Weihs[a,b,e,h]

[a] *Department of Materials Science and Engineering, Johns Hopkins University, 3400 N Charles St, Baltimore, 21218, MD, U.S.A*
[b] *Hopkins Extreme Materials Institute, Johns Hopkins University, 3400 N Charles St, Baltimore, 21218, MD, U.S.A*
[c] *Department of Chemical and Biomolecular Engineering, Johns Hopkins University, 3400 N Charles St, Baltimore, 21218, MD, U.S.A*
[d] *Kevin T. Crofton Department of Aerospace and Ocean Engineering, Virginia Tech, 1600 Innovation Drive, Blacksburg, 24061, VA, U.S.A*
[e] *Department of Mechanical Engineering, Johns Hopkins University, 3400 N Charles St, Baltimore, 21218, MD, U.S.A*
[f] *Department of Biomedical Engineering, Johns Hopkins University, 3400 N Charles St, Baltimore, 21218, MD, U.S.A*
[g] *Research and Development, Fort Wayne Metals Research Products Corp, 9609 Ardmore Ave, Fort Wayne, 46809, IN, U.S.A*
[h] *Translational Tissue Engineering Center, Johns Hopkins School of Medicine, 400 N Broadway, Baltimore, 21231, MD, U.S.A*

Abstract

Over the past decade, the application of artificial intelligence (AI) tools has accelerated the discovery of novel material compositions, but has done little to speed the discovery of novel material processing paths, particularly when sequential processing operations are required. Current process optimization often involves extensive efforts to characterize microstructures and properties to fully understand process-microstructure-property relationships. However, characterizing both microstructures and properties slows and limits the scalability of materials optimization. Here, we demonstrate that processing pathways can be optimized within an AI-driven closed loop *without* the need for intermediate microstructural characterization. By varying processing steps and parameters in a controlled manner and focusing on properties that can be quantified rapidly, our multi-objective framework simultaneously targets two competing properties: resistance to deformation (hardness) and resistance to corrosion (corrosion rate). We demonstrate this approach in ZX10, a lean, biodegradable magnesium alloy with potential applications in temporary orthopedic implants. Within three closed-loop iterations, the framework identifies processing pathways that move beyond the hardness–corrosion trade-off observed in the initial dataset, achieving high hardness and low one-day corrosion rates. Subsequent mechanical testing and extended corrosion experiments confirm that the optimized materials also exhibit increased tensile strength, enhanced ductility, and favorable corrosion performance over 14 days. Post-optimization microstructural characterization reveals that the selected materials share similar microstructural features, including ultrafine grains, comparable dislocation densities and crystallographic textures, and finely dispersed second-phase particles. These findings demonstrate that rapidly measured properties can guide the identification of favorable processing conditions without requiring microstructural information during optimization, while subsequent characterization provides insight into the underlying structure–property relationships. By delaying resource-intensive microstructural characterization until promising processing conditions are identified, this framework substantially reduces the experimental burden and offers a scalable strategy for AI-driven materials processing.

Introduction and Design Hypothesis

The application of artificial intelligence (AI) has transformed the search for new material compositions and crystal structures over the past ten years, but it has had far less impact on discovering novel processing routes. [1–6] This is critically important for the field because composition alone does not determine material properties. Every predicted material must still be processed into a physical form that delivers the intended properties. [5, 7] Materials processing is also path-dependent: the outcome of each operation depends on the physical state inherited from preceding steps; changing the order of otherwise similar operations can produce different microstructures and properties. [8, 9] Temperature, strain, time, and other processing variables cannot always be treated independently when they are present in the process. The complete, ordered processing pathway must itself be treated as the overarching design variable.

This pathway-level view differs from the typical application of AI to materials processing. Most reported studies optimize parameters within a predetermined operation or fixed processing route rather than navigating alterna-

*Corresponding authors
Email addresses: sreenivas.raguraman@mat.ethz.ch (Sreenivas Raguraman), msharmap@vt.edu (Maitreyee Sharma Priyadarshini)
[1] Present address: Laboratory of Metal Physics and Technology, Department of Materials, ETH Zürich, 8093 Zürich, Switzerland.

tive multi-step histories. Machine learning approaches have been applied to optimize rolling, heat treatment, and additive-manufacturing conditions, but these studies have largely focused on adjusting parameters within predefined processing routes rather than optimizing the processing pathways themselves. [6, 10–12] Similarly, adaptive experimentation has enabled closed-loop optimization of feasible manufacturing conditions within a fixed process. [13] Although recent approaches have proposed treating complete synthesis protocols as design variables, [14] the closed-loop experimental optimization of processing pathways remains relatively underexplored.

While important to materials optimization, pathway-level navigation creates a second challenge: How much information must be acquired before the next experiment can be selected? Process–structure–property models have shown that microstructural descriptors can improve predictions, [15] and microstructure-aware Bayesian optimization explicitly incorporates structural information during experimental selection. [16] Other closed-loop frameworks similarly combine optimization with substantial physical information; the "Birdshot" code base, for example, integrates multi-objective Bayesian optimization with thermodynamic screening, predicted stacking-fault energy, and extensive experimental characterization. [17] Self-driving laboratories can accelerate experimentation through automation, [18] but many rely on predefined workflows that constrain the flexibility to modify processing steps and their sequence between experimental iterations. Moreover, automation accelerates data acquisition without necessarily reducing the amount of information required to guide optimization. For bulk materials, microscopy, crystallographic mapping, and phase analysis can require substantial specimen preparation, instrument time, and expert interpretation. [19, 20] Requiring these measurements for every candidate can therefore make characterization a major bottleneck to rapid optimization.

An alternative explored here eschews detailed and costly microstructural characterization until after AI-guided down-selection to a small promising set of candidates. At fixed composition and from a controlled starting condition, rapidly measured properties provide integrated feedback on the material state produced by each processing pathway. These responses can potentially guide the next experiment without supplying the model with intermediate microstructural information. Detailed characterization can then follow once promising pathways are identified. This decouples two tasks that we hypothesize need not occur at the same pace: navigating toward useful processing conditions and understanding how the resulting microstructures dictate the measured properties. While microstructure remains essential for understanding the final states, we contend that they are not needed to identify the processing routes that yield the required properties.

Biodegradable magnesium alloys provide a suitably stringent model system to test this strategy because their useful performance/deployment requires two competing responses to be controlled simultaneously. Unlike permanent implant metals, biodegradable Mg alloys are intended to provide temporary mechanical support and then dissolve once that support is no longer required. [21–23] This behavior makes them attractive for orthopedic fixation devices and cardiovascular scaffolds, where avoiding permanent hardware can reduce long-term complications and eliminate secondary removal procedures. Magnesium is also lightweight, biocompatible, and has an elastic modulus closer to that of bone than conventional implant metals. [24, 25] Its degradability, however, creates a demanding design problem: the material must retain sufficient mechanical integrity during healing while degrading at an appropriate rate. Mechanical performance and corrosion must therefore be optimized together.

Mechanical performance and corrosion in ZX10 alloy are strongly coupled, and improving one can come at the expense of the other. Processing alters grain structure, crystallographic texture, dislocation density, solute distribution, and precipitate populations, all of which influence both strength and corrosion. [22, 26] Previous work has shown that severe plastic deformation can increase hardness and strength while accelerating corrosion, whereas subsequent thermal treatment can shift this balance. [26–28] The resulting properties therefore depend strongly on both the processing sequence *and* its conditions. Identifying which combinations of strain, strain rate, temperature, and duration produce a favorable hardness–corrosion balance for the ZX10 alloy, therefore, constitutes a path-dependent, multi-objective search problem.

To test whether multi-step processing pathways can be optimized using property feedback alone, we developed an AI-driven, multi-objective closed loop in which controllable ZX10 Mg alloy processing descriptors define the search space and rapid hardness and short-duration corrosion measurements guide experimental selection across three learning rounds. No microstructural descriptors or intermediate microstructural measurements enter model training or candidate selection. Detailed characterization is, instead, reserved for down-selected conditions. We therefore asked whether experimentally feasible multi-step processing pathways can be navigated using only processing descriptors and rapid property feedback, while reserving detailed microstructural characterization for post-search explanation and validation.

Processing generates a broad property landscape at fixed composition

Alloy chemistry alone does not dictate performance. We assembled an initial dataset of 40 experimentally realized ZX10 alloy conditions spanning extrusion, equal-channel angular pressing (ECAP), rolling, solution treatment, and subsequent thermal treatments. (Figure 1a,b) Each condition was represented by its complete processing history, including strain, strain rate, treatment temperature, treatment duration, and the order of operations. The design

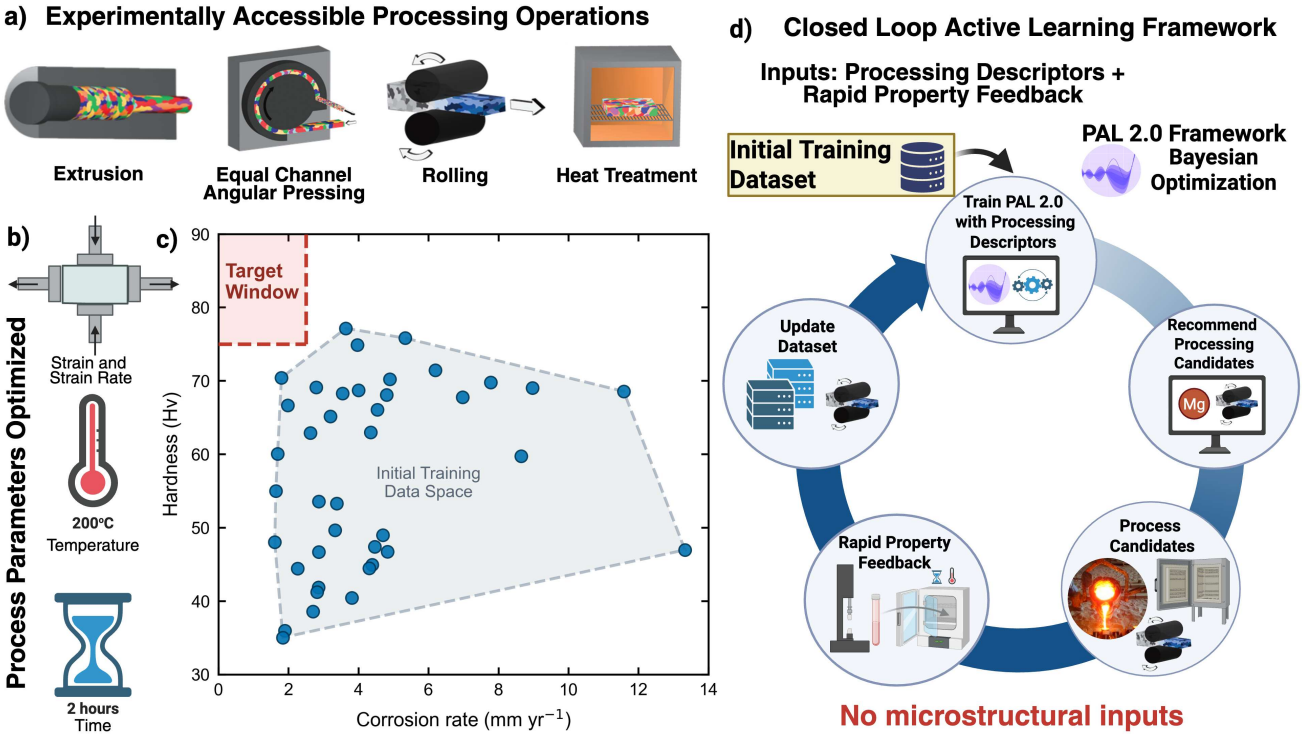


Figure 1: **Processing-pathway design space and closed-loop framework at fixed composition.** **a,** Experimentally accessible thermomechanical operations used to construct ZX10 processing pathways, including extrusion, equal-channel angular pressing, rolling, and heat treatment. **b,** Processing descriptors used to represent each ordered pathway, including strain, strain rate, temperature, and treatment duration. **c,** Hardness and 24-h corrosion rate measured for the 40 conditions in the initial dataset. The upper-left window marks the predefined target region of high hardness and low corrosion. **d,** Closed-loop framework used to recommend, realize, and evaluate new processing pathways using measured property feedback. Created in BioRender. Raguraman, S. (2026) https://BioRender.com/ebucykw

space thus consisted of experimentally realized processing histories rather than arbitrary combinations of independently varied parameters.

We mapped this processing space using hardness and 24-h corrosion rate measurements as rapid feedback variables for mechanical and degradation performance. Hardness served as a surrogate for tensile strength, for which an established relationship exists in ZX10. [28] Degradation was quantified by immersion, as unstable surface films and localized attack can complicate electrochemical estimates of Mg corrosion rates. [29, 30] Our previous work identified CO_2-buffered Earle's Balanced Salt Solution (EBSS) at 37 °C as a controlled and comparatively aggressive environment suitable for preliminary screening [23]. A 24-h exposure provided sufficient differentiation among processing conditions while retaining the turnaround required for swift, iterative experimentation. It was therefore used as a screening measure, with longer-duration degradation reserved for post-search validation.

Despite the unchanged alloy chemistry, the 40 processing histories produced a broad property landscape (Figure 1c). Hardness ranged from 35.0 to 77.2 HV, while the 24-h corrosion rate varied from 1.61 to 13.33 mm yr^{-1}. Processing alone, therefore, generated more than a two-fold variation in hardness and an approximately eight-fold variation in corrosion rate. The complete processing histories and measured responses for all 40 conditions are provided in the Supplementary Results (SI 1.1).

This landscape also exposed the difficulty of improving both responses simultaneously. Highly deformed conditions tended to combine high hardness with rapid corrosion, whereas several of the lowest-corrosion states exhibited substantially lower hardness. This behavior is consistent with the coupled effects of deformation and thermal exposure previously observed in ZX10 alloy. [26, 28] Deformation can increase hardness through grain refinement and defect accumulation, while the resulting highly strained state can also accelerate initial corrosion. Subsequent thermal treatments can reduce stored strain and alter solute and precipitate distributions, improving corrosion resistance while relaxing part of deformation-induced strengthening. Processing history therefore shifted both responses strongly, but not necessarily in the same direction.

To define the objective for closed-loop exploration, we specified the target region shown in Figure 1c: hardness above 75 HV and a 24-h corrosion rate below 2.5 mm yr^{-1}. The hardness threshold lies near the upper boundary of the initial dataset and corresponds to an estimated ultimate tensile strength of approximately 240–260 MPa. [31] The corrosion threshold selected the low-corrosion tail of the initial response and was defined specifically for the 24-h

EBSS screening condition. Because absolute Mg corrosion rates depend strongly on medium composition, buffering, exposure duration, and solution volume, this threshold was not intended as a universal long-term or in-vivo degradation limit. [23] Within this screening environment, it imposed a stringent criterion for retaining the strengthening introduced by processing while suppressing its associated corrosion response. None of the 40 initial conditions occupied this region.

This unoccupied region provided a clear target for closed-loop exploration. We implemented PAL 2.0 using the ordered processing histories and their measured hardness and 24-h corrosion responses. (Figure 1d) [32, 33] The subsequent search tested whether iterative model-guided experimentation could move beyond the hardness–corrosion trade-off represented by the initial data set and identify experimentally executable processing pathways that yielded high hardness with low corrosion.

Closed-loop navigation beyond the initial trade-off

We tested the closed-loop framework through three successive experimental rounds, adding 11 conditions (effectively data points) to the initial 40-state processing–property landscape (Figure 2a,b). The search received two forms of experimental feedback: Measured hardness and 24-h corrosion redirected the model toward more favorable property combinations, while prescribed versus achieved processing revealed which regions of the nominal processing space were physically and practically accessible. Across the three rounds, the search first extended the accessible hardness, then improved both properties, and finally reduced corrosion while retaining high hardness. By Round 3, two processing conditions produced properties that overlapped the predefined target region within experimental uncertainty.

The first round of AI predictions used broad processing bounds and a single hardness-to-corrosion-rate ratio as the optimization objective. All four recommended conditions exceeded the maximum hardness of the initial dataset, reaching 78.8–85.1 HV compared with the initial maximum of 77.2 HV. Their corrosion rates, however, remained between 5.9 and 6.1 mm yr^{-1} and well outside the target region. The combined ratio had therefore favored gains in hardness without requiring a corresponding reduction in corrosion. Before Round 2, we replaced the H/CR ratio objective with separate hardness and corrosion objectives so that improvement in one property could no longer compensate for a lack of improvement in the other.

The first round also exposed a second limitation: the nominal candidate space extended beyond what was experimentally useful. Several prescribed deformation steps could not be fully realized, particularly during the second deformation stage (Figure 2c), while the broad initial bounds permitted thermal treatments that were experimentally feasible but impractically long. These recommendations were informative rather than simply unsuccessful. The observed deformation limits were used to contract the allowable strain bounds, and the permitted thermal-treatment durations were shortened before the next round. Round 1 therefore changed both what the model optimized and the region of processing space within which it searched.

Refining both the objective and the accessible processing space produced a marked shift in Round 2. Hardness increased to 87.2–100.5 HV, such that even the lowest Round 2 value exceeded the highest value obtained in Round 1. At the same time, corrosion decreased to 3.4–4.7 mm yr^{-1}, with the highest Round 2 value remaining below the lowest measured in Round 1. One condition reached 100.5 HV, approximately 30% above the maximum hardness of the initial dataset, while another combined 92.65 HV with a corrosion rate of 3.44 mm yr^{-1}. The AI-predicted, experimentally observed boundary had therefore moved simultaneously toward higher hardness and lower corrosion (Figure 2b).

The Round 2 experiments also clarified the remaining feasibility constraints. All first-stage rolling reductions were achieved close to their prescribed values, whereas none of the second-stage reductions reached their recommended values. This distinction indicated that the deformation limits depended on the position of rolling within the processing sequence, allowing the upper strain bound for the second rolling stage to be refined independently before Round 3. In parallel, LASSO-based analysis of the experimental data revealed distinct associations between processing descriptors and the two property responses (Supplementary Fig. S1). The final heat-treatment temperature exhibited the largest coefficient magnitude for corrosion rate, whereas hardness was most strongly associated with the rolling strains, particularly that of the second rolling stage. These findings informed the final optimization round, which incorporated the refined processing bounds and a LASSO-inspired linear prior in the corrosion-rate GP model.

With the remaining feasibility constraint localized and the corrosion-rate surrogate model updated, Round 3 asked whether corrosion could be reduced further without sacrificing the high-hardness regime reached in Round 2. All recommended deformation and thermal-treatment steps were realized as prescribed, allowing all three pathways to be implemented in full (Figure 2c). The recommendations included sequences in which rolling was followed by thermal treatment and further rolling, together with terminal treatments at 50 °C, the lower temperature bound of the search space. The resulting hardness values for R3-R1, R3-R2, and R3-R3 were 95.5, 88.4, and 86.2 HV, respectively, with corresponding corrosion rates of 3.07, 2.40, and 2.62 mm yr^{-1}. The principal change in the final round was therefore a further reduction in corrosion while maintaining high hardness; indeed, two conditions overlapped the predefined target region within experimental uncertainty.

Agreement between model predictions and experimental

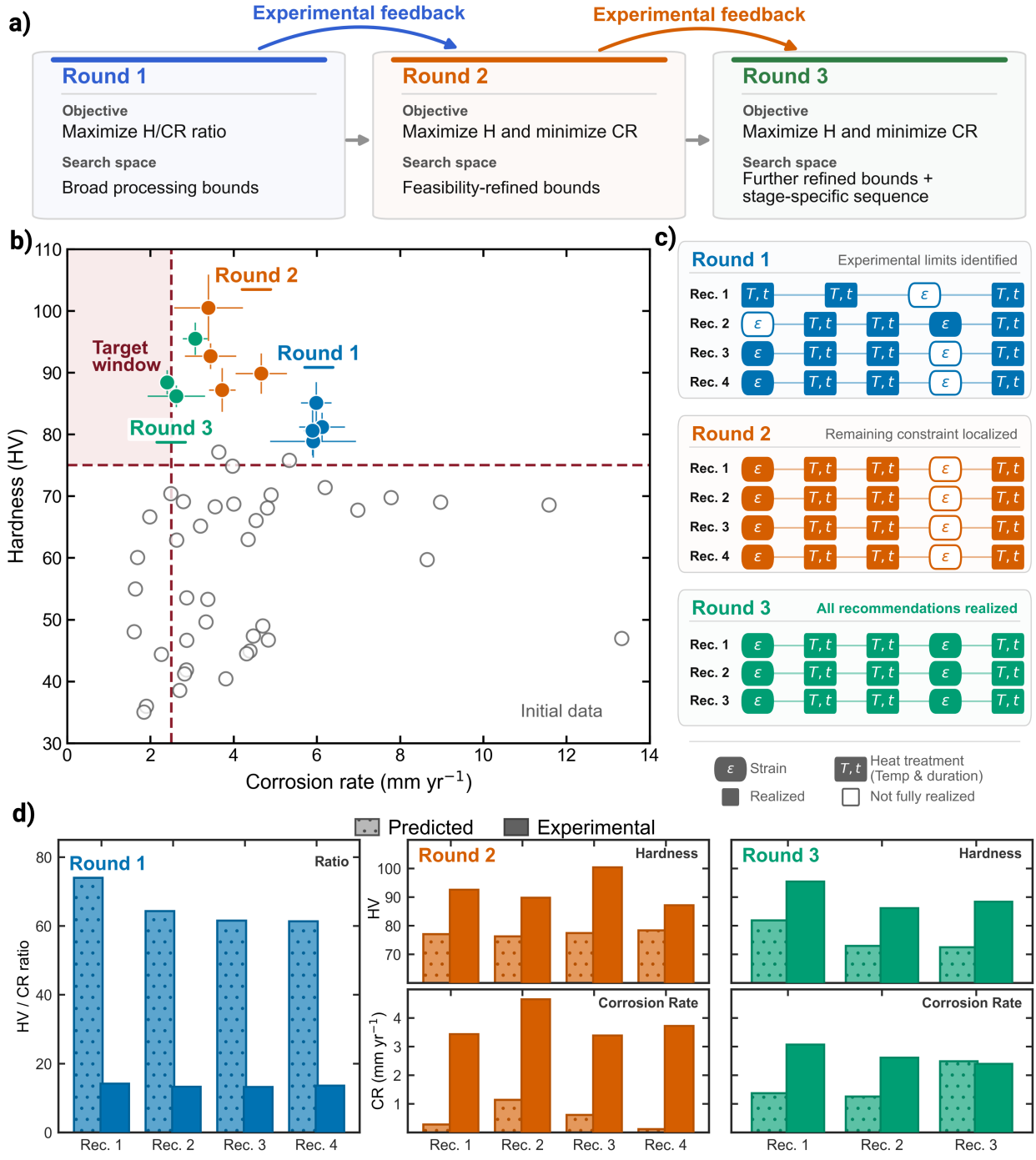


Figure 2: **Closed-loop navigation progressively advances towards a targeted, experimentally observed hardness–corrosion boundary. a:** Evolution of the closed-loop search across three experimental rounds, transitioning from a single hardness-to-corrosion-rate ratio and broad processing bounds in Round 1, to separate property objectives and feasibility-refined bounds in Round 2, followed by further refined processing bounds and a LASSO-inspired prior for the corrosion-rate surrogate model in Round 3. **b:** Evolution of the measured hardness–corrosion landscape. Open symbols denote the initial 40-state dataset, and colored symbols denote conditions evaluated during Rounds 1–3. Dashed boundaries indicate the predefined target region, and error bars represent standard deviations. Successive rounds advance the measured boundary toward higher hardness and lower corrosion. **c:** Experimental realization of the recommended processing sequences. Filled symbols indicate operations implemented as prescribed, whereas outlined symbols indicate deformation steps that could not be fully realized. Experimental feedback progressively localized the feasibility constraints, to the extent that all Round 3 recommendations were realized as prescribed. **d:** Comparison of model-predicted and experimentally measured responses for the recommended conditions. Round 1 used a ratio-based objective, whereas Rounds 2 and 3 treated hardness and corrosion separately. Created in BioRender. Raguraman, S. (2026) https://BioRender.com/ebucykw

measurements differed between the two properties (Figure 2d). Hardness was predicted more consistently than corrosion, whereas individual corrosion values remained more difficult to resolve from the compact dataset. Exact pointwise prediction was not required, however, for the model to guide useful experimental decisions. Across 11 processing recommendations, the resulting properties moved progressively toward the target region while feasibility feedback continuously corrected the accessible search space. The value of the closed loop therefore lay not in reproducing every measured response exactly, but in using each experimental round to improve where the search looked next.

In summary, the closed-loop campaign expanded the dataset from 40 to 51 experimentally realized processing conditions and reached a desirable property region inaccessible by the initial dataset. Condition-level processing histories, model predictions, measured responses, and prescribed-versus-achieved deformation are provided in the Supplementary Results (SI 1.1-1.3). Having established that the property-guided search could move beyond the initial trade-off, we next examined the microstructures of the two promising AI-optimized conditions to identify the structural features associated with their favorable hardness–corrosion balance.

AI-guided processing converges on a common microstructural window

Candidates R3-R2 and R3-R3 were selected for post-search microstructural characterization because both overlapped the predefined target region within experimental uncertainty. We compared their grain size and morphology, crystallographic textures, retained defect states, and second-phase populations to determine whether the two selected conditions had also converged toward a common microstructural state.

We determined that the two pathways had converged remarkably closely in processing space (Figure 3a,b). Both comprised ECAP, 1% cold rolling, thermal treatment at 196 °C, a secondary 2% rolling reduction, and a terminal 50 °C treatment, differing only in the duration of the final step: 10 h for R3-R2 and 12 h for R3-R3. Because no constraint required the recommended pathways to resemble one another, their convergence suggests that the closed loop had localized a narrow processing window associated with the targeted hardness–corrosion balance.

The EBSD maps revealed ultrafine-grained structures in both selected states, with strongly overlapping grain-size distributions and predominantly equiaxed to mildly elongated morphologies (Figure 3c,e,j). Increasing the duration of the terminal 50 °C treatment from 10 to 12 h produced little change in either grain size or morphology, indicating that both pathways remained within the same refined grain regime. The microstructures are consistent with ECAP providing the principal grain-refinement step, while the subsequent mild rolling reductions introduced additional deformation without producing the strongly elongated morphology associated with heavier rolling. Retention of this refined structure, together with the additional deformation introduced during rolling, is consistent with the high hardness measured in both conditions.

The similarity extended beyond grain morphology: The 0001 pole figures were closely comparable (Figure 3d,f), and the geometrically necessary dislocation (GND) densities occupied the same broad range with substantial overlap in their distributions (Figure 3j). Thus, the two pathways converged not only towards similar grain morphologies, but also on comparable texture and retained deformation states. This combination is relevant to the targeted property balance. Grain refinement and retained deformation contribute to strengthening, whereas highly strained states in Mg alloys can also increase electrochemical heterogeneity and accelerate localized corrosion. [28, 34] The selected conditions retained deformation-related strengthening without remaining in the highly strained regime associated with the fastest corrosion response.

Their ordered processing histories help explain how this balance was reached. ECAP and the initial rolling step established a refined, defect-containing structure, after which thermal exposure near 196 °C provided an opportunity for recovery and secondary-phase evolution without extensive grain growth, consistent with previous observations in ECAP-processed ZX10. [26] The subsequent 2% rolling reduction then reintroduced a limited amount of strain before the final low-temperature treatment. The close agreement in grain structure and GND density after 10 and 12 h at 50 °C indicates that both terminal treatments remained within the same grain and defect regime. The complete sequence therefore combined repeated deformation and thermal exposure while preserving the refined structure established earlier in the pathway.

The BSE images revealed another feature shared by the selected states: a fine, closely spaced second-phase population distributed throughout the Mg matrix (Figure 3g,h). The observed fields were not dominated by sparse coarse particles or pronounced particle-rich and particle-poor regions. Such a distribution can influence both sides of the hardness–corrosion balance. Fine second phases can provide additional barriers to dislocation motion, whereas their size and spatial distribution determine how strongly local galvanic coupling is concentrated. Coarse or spatially heterogeneous cathodic particles can intensify localized dissolution of the surrounding Mg matrix, while a finer and more broadly distributed population reduces the spatial contrast in electrochemical activity. Previous work on ZX10 similarly associated a more homogeneous $Ca_2Mg_6Zn_3$ distribution and reduced prevalence of coarse Mg_2Ca particles with improved corrosion resistance after thermal treatment. [26]

The X-ray diffraction patterns provide complementary evidence that the convergence extended to the phase state (Figure 3i). Both patterns were dominated by α-Mg reflections and contained detectable reflections consistent with

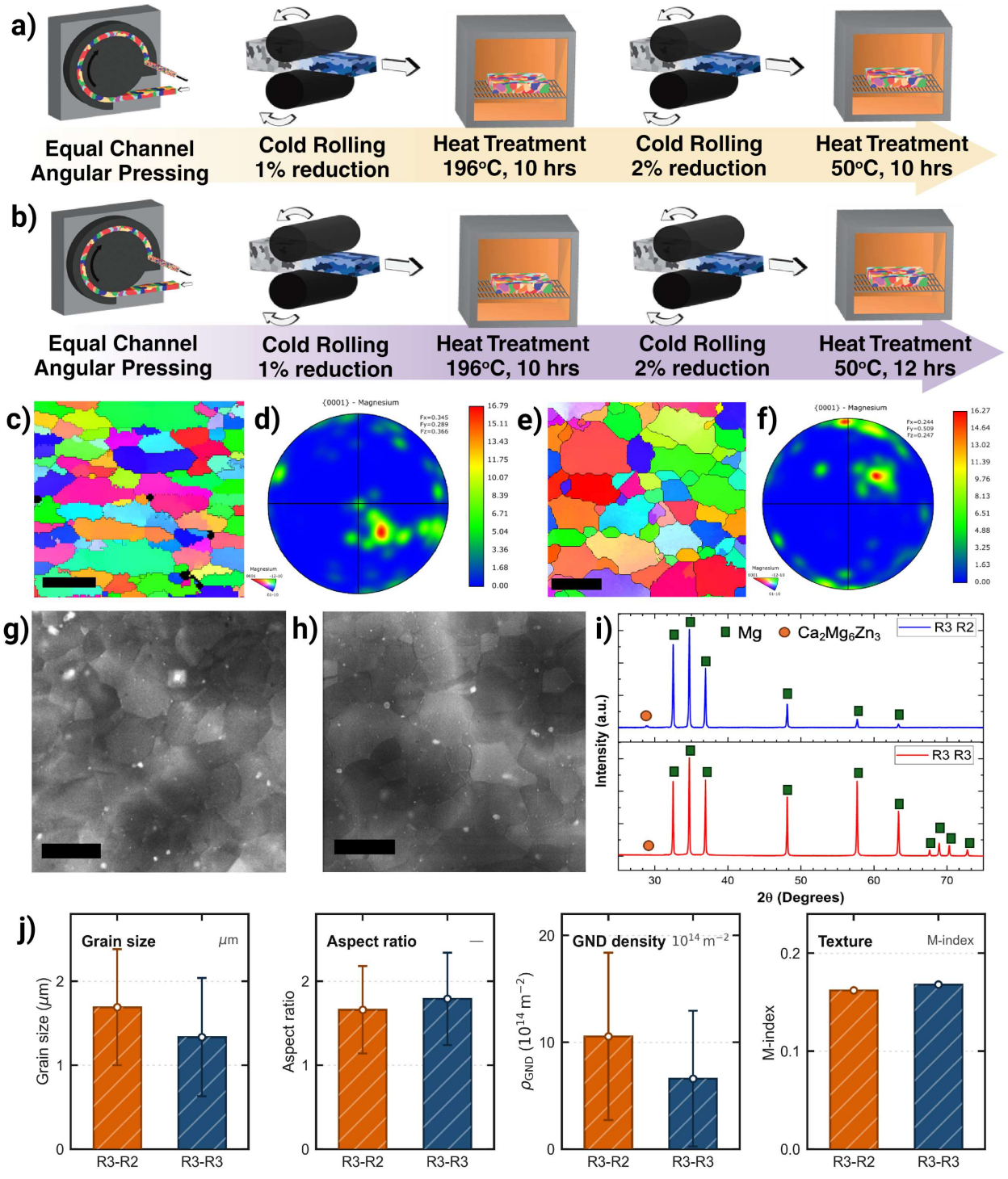


Figure 3: **AI-guided processing converged to a common microstructural window. a,b:** Processing pathways corresponding to the two Round 3 states selected for targeted structural characterization, R3-R2 and R3-R3. The pathways differ only in the duration of the final 50 °C thermal treatment. **c,e:** EBSD orientation maps showing the refined grain structures of R3-R2 and R3-R3, respectively. **d,f:** Corresponding 0001 pole figures showing their crystallographic textures. **g,h:** Backscattered-electron micrographs showing fine, closely spaced second-phase particles within the Mg matrix. **i:** X-ray diffraction patterns comparing the phase constitution of R3-R2 and R3-R3. **j:** Quantitative comparison of grain size, grain aspect ratio, geometrically necessary dislocation density and texture intensity. Despite being identified without microstructural input, the two selected states occupy a common microstructural window characterized by ultrafine grains, comparable grain morphology, texture and defect states, and dispersed fine second-phase features. Scale bars are 2 μm. Created in BioRender. Raguraman, S. (2026) https://BioRender.com/ebucykw

$Ca_2Mg_6Zn_3$. Together with the BSE observations, these results support the presence of similar Ca–Mg–Zn second-phase populations in the two selected conditions. Extending the final 50 °C treatment from 10 to 12 h did not produce a major change in the phase constitution resolved by XRD.

Taken together, R3-R2 and R3-R3 converged across several levels of microstructure. Both retained ultrafine grains, comparable texture and deformation states, and fine, broadly distributed second-phase populations. No single descriptor alone explains the measured hardness–corrosion balance. Rather, the selected processing window produced a combination of grain, defect, texture, and second-phase states that collectively supported high hardness while avoiding the microstructural extremes associated with rapid corrosion. More detailed analyses of grain-size and morphology distributions, grain-boundary misorientation, GND-density distributions, second-phase composition, and phase constitution are provided in the Supplementary Results (SI 1.4).

Importantly, this microstructural convergence was established only after the property-guided search had identified the selected pathways. The remaining question was whether these states were favorable only according to the rapid hardness and 24-h corrosion metrics used during navigation, or whether their advantages extended to more complete measures of material performance. We therefore evaluated their tensile behavior and longer-duration degradation across multiple testing environments.

Performance extends beyond the optimization objectives

A central risk of optimization using rapid proxy measurements is that apparent improvements may not persist under more complete evaluation. The closed-loop search targeted high hardness and low 24-h corrosion in EBSS; tensile strength, ductility, toughness, and longer-duration corrosion in other environments were not optimization objectives. We therefore used these "out-of-loop" measurements to determine whether the selected processing window remained favorable when evaluated beyond the quantities used to guide the search.

To anchor this validation, we compared R3-R2 and R3-R3 against conditions spanning the initial processing landscape. The solution-treated state (ST) combined the lowest hardness with low corrosion, ST-R375A1 represented extreme conditions of high corrosion, and ECAP+150A10 provided an additional deformed and thermally treated reference. Together, these conditions captured the central trade-off observed in the initial data set between mechanical performance and corrosion resistance.

The hardness gains translated directly to tensile strengthening (Figure 4a,b). Mean ultimate tensile strength increased from 130.2 ± 16.4 MPa for ST to 206.2 ± 30.2 MPa for R3-R2 and 216.9 ± 37.2 MPa for R3-R3, corresponding to gains of 58% and 67%, respectively. Importantly, this strengthening was not accompanied by a loss of tensile ductility. Mean strain to failure was 13.7 ± 1.7% for ST, compared with 18.0 ± 1.5% for R3-R2 and 23.8 ± 8.1% for R3-R3, although the latter showed greater specimen-to-specimen variability. The representative curves further show that both selected states continued to strain-harden over an extended deformation interval rather than reaching higher strength at the expense of premature failure.

The combined increase in strength and retained deformation capacity produced a substantial increase in the energy absorbed before fracture. Tensile toughness rose from 14.5 ± 4.3 MJ m^{-3} for ST to 35.7 ± 7.1 and 46.3 ± 5.6 MJ m^{-3} for R3-R2 and R3-R3, respectively, corresponding to 2.5- and 3.2-fold increases. These gains arose from sustaining higher stresses across a larger deformation interval rather than from peak strength alone. This response is consistent with the microstructural window identified above, in which ultrafine grains and retained deformation provided strengthening while the thermally evolved defect and second-phase states preserved substantial plastic deformation. More detailed comparisons of strain hardening, deformation behavior, and fracture-surface morphology are provided in the Supplementary Results (SI 1.5).

Next, we tested whether the corrosion response remained favorable beyond the 24-h EBSS screening condition. This comparison is particularly important for Mg alloys because degradation rates depend strongly on medium composition, buffering, exposure duration, and the corrosion-product layers that develop during immersion [23]. Fourteen-day testing in EBSS, HBSS, and DMEM therefore challenged the selected states across both longer exposure times and distinct chemical environments (Figure 4c).

The surrounding medium had a pronounced effect on the absolute corrosion rate. Across the tested conditions, corrosion in EBSS was approximately four times that measured in DMEM, while rates in HBSS were approximately twice those in DMEM. Despite this strong environmental dependence, the relative placement of the processing conditions remained consistent. ST exhibited the lowest corrosion rate and ST-R375A1 the highest in all three media, while R3-R2 and R3-R3 remained between these extremes and below the high-corrosion reference. In EBSS, both selected states corroded more slowly than ECAP+150A10. The corresponding post-corrosion morphologies likewise reflected the strong influence of medium chemistry and are examined in greater detail in the Supplementary Results (SI 1.6).

The selected states did not minimize corrosion in isolation, nor was that the objective. ST retained the lowest corrosion rate, but it also exhibited the lowest hardness and tensile strength. R3-R2 and R3-R3 instead combined 58–67% higher tensile strength, substantial retained ductility, 2.5–3.2-fold greater tensile toughness, and cor-

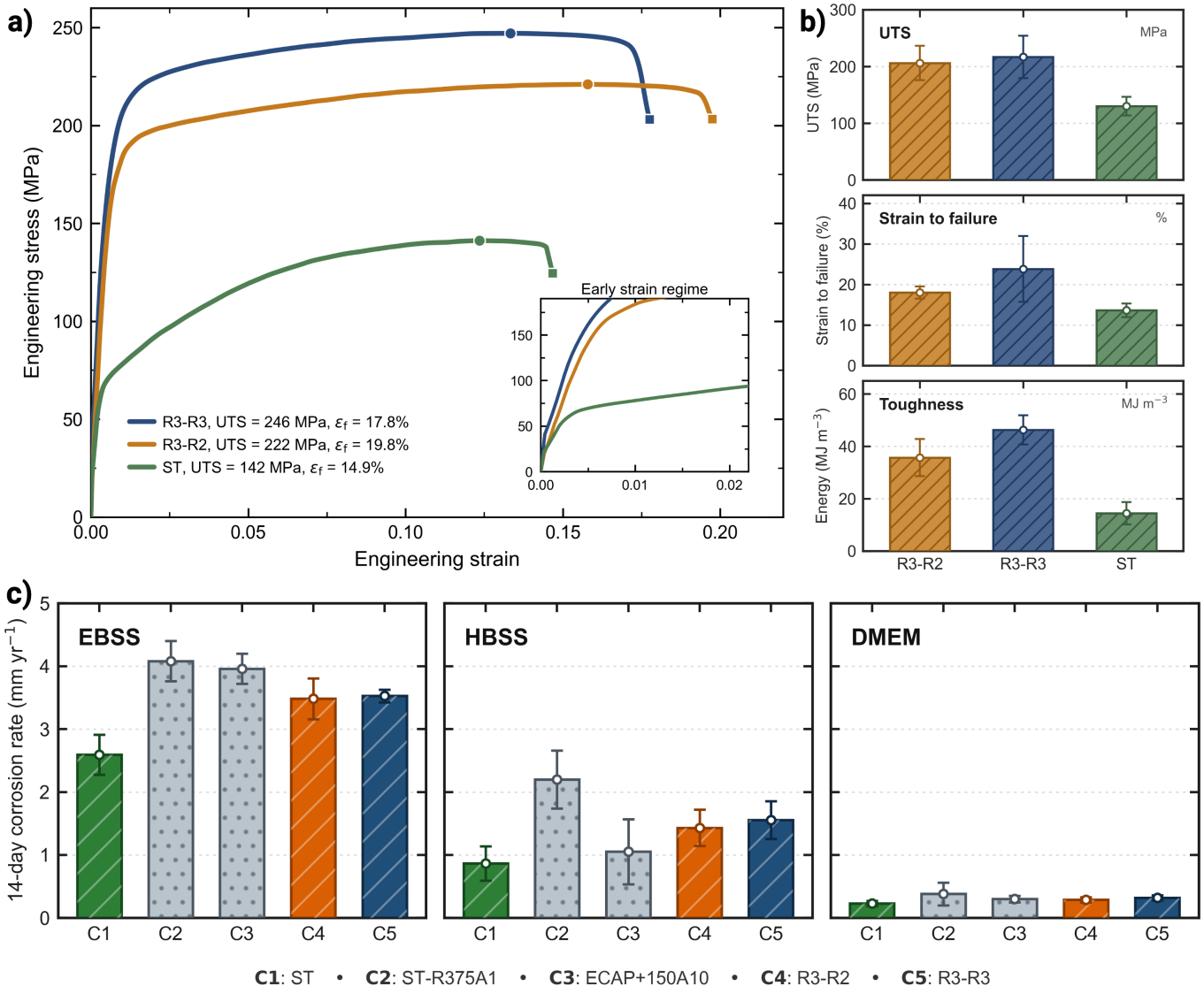


Figure 4: **Performance of the closed loop-selected states beyond the optimization objectives. a:** Representative engineering stress–strain curves for R3-R2 and R3-R3 compared with the solution-treated reference state (ST). The inset highlights the early-strain regime. Ultimate tensile strength (UTS) and strain to failure (ε_f) for the representative curves are indicated. **b:** Mean ultimate tensile strength, strain to failure, and tensile toughness for R3-R2, R3-R3, and ST. Tensile toughness was calculated from the area under the engineering stress–strain curve. All conditions were evaluated using identical specimen geometry. Bars represent mean values and error bars indicate standard deviation. **c:** Corrosion rates measured after 14 days of immersion in Earle's Balanced Salt Solution (EBSS), Hank's Balanced Salt Solution (HBSS) and Dulbecco's Modified Eagle Medium (DMEM). C1–C5 denote ST, ST-R375A1, ECAP+150A10, R3-R2 and R3-R3, respectively. ST and ST-R375A1 represent the low- and high-corrosion extremes of the initial processing landscape. Bars represent mean values and error bars indicate standard deviation ($n = 5$). Tensile properties and 14-day corrosion rates were measured after completion of the closed-loop search and were not supplied as optimization objectives. Created in BioRender. Raguraman, S. (2026) https://BioRender.com/ebucykw

rosion rates that remained well removed from the high-corrosion extreme across all three environments. The improvements identified using hardness and short-duration corrosion therefore persisted across properties and testing conditions that were never supplied to the closed loop, showing that the selected processing window extended beyond the two responses used during optimization.

Conclusions and Outlook

The central implication of this study is that effective closed-loop materials processing does not need to rely on collecting the maximum possible amount of information from every experiment. To be more specific, for pathway-dependent problems, the limiting cost is invariably not the cost of computational search itself but the experimental burden required to generate each new data point. Here, we

demonstrate that processing steps and parameters, combined with rapidly measured hardness and 24-h corrosion rates, provide sufficient information to guide closed-loop optimization. This compact information set was sufficient to move the search beyond the initial hardness–corrosion trade-off and toward experimentally realizable processing conditions, importantly, *without requiring costly intermediate microstructural characterization*.

The resulting reduction in experimental burden was substantial. A retrospective workload analysis, detailed in Supplementary Results (SI 1.7), estimates that applying detailed characterization only after down-selection avoided approximately 200–300 hours of hands-on researcher time relative to applying the same characterization package to all 51 experimentally evaluated states. This estimate excludes unattended processing, immersion periods, and automated acquisition and therefore represents active researcher effort rather than total calendar time. Hence, the 200–300 hours is almost certainly a conservative estimate of gained productivity. The significance of this comparison is not that conventional studies necessarily characterize every condition but that closed-loop experimentation introduces a repeated decision point: What information must be acquired before the next experiment can be selected? Reducing that per-condition information burden can be as important as reducing the number of experiments themselves.

This strategy was possible because the alloy chemistry and initial material state were controlled. Under these conditions, processing modified the material state, and the resulting mechanical and corrosion responses integrated the consequences of those changes. We found that hardness and short-duration corrosion tests were sufficient to guide navigation even though the model did not include information regarding grain structure, texture, defect density, solute distribution, or phase constitution. These quantities remain essential for interpreting the selected states, but they were not required to identify them. The distinction is important: microstructural characterization need not be removed from materials discovery, but it need not occupy every iteration of the search. Rapid measurements can support navigation, while detailed characterization can be reserved for explanation and validation once the search has identified where deeper understanding is most valuable.

The results also challenge the idea that the usefulness of a closed-loop model should be judged primarily by pointwise predictive accuracy. The model did not reproduce every measured response precisely, particularly for corrosion, yet the complete model–experiment loop progressively moved toward more favorable property combinations and more experimentally realizable pathways. Recommendations that could not be implemented as prescribed should not be relegated to designation as failed experiments. They revealed where the nominal processing space departed from the physically accessible one. That information was used to revise deformation limits, remove impractically long treatments, and represent processing variables according to their position within the sequence. For materials processing, feasibility is therefore not only a constraint to impose before optimization; it can itself be learned experimentally as the search proceeds. This becomes increasingly important when manufacturing constraints such as achievable deformation, treatment duration, equipment capability, throughput, energy use and cost are considered alongside material performance.

A natural extension to our completed study would be to make the information burden itself adaptive. Rapid proxy measurements could provide feedback for most candidates, while higher-fidelity measurements such as microscopy, diffraction, or spectroscopy could be requested only when the available information was no longer sufficient to distinguish among promising regions of the search space. Detailed characterization would then become another selectable experiment rather than a fixed requirement applied uniformly to every condition. In such a multi-fidelity framework, the closed loop would decide not only which material condition should be produced next, but also which measurement would provide the most useful information for the next decision.

The broader principle we have uncovered is not specific to magnesium alloys or, indeed, to our Bayesian PAL 2.0 approach. Path-dependent design spaces occur wherever material performance depends on an ordered sequence of controllable operations, including additive manufacturing, processing for polymers, ceramics and semiconductors, as well as other thermomechanical manufacturing routes. The relevant descriptors, rapid measurements, and feasibility limits will differ across systems, but the same principle can apply: represent the processing history explicitly, use the fastest measurements that capture the targeted performance, and update the accessible search space as experiments reveal what can actually be realized. The transferable contribution is therefore not a particular surrogate model or property measurement, but a strategy for allocating experimental information according to its value for the next decision.

This perspective also exposes a limitation of current materials data. Complete processing histories are rarely reported consistently enough to reconstruct a path-dependent design space from the literature. Labels such as "rolled," "annealed," or "solution-treated" often omit essential details necessary for reproducibility of published results, such as order of operation, intermediate states, strain rate, treatment duration, solvent blend compositions, deviations from prescribed conditions, and unsuccessful processing attempts. For pathway-dependent materials design, these details are not secondary metadata; they *define* the material condition itself. The present results show that useful closed-loop guidance can nevertheless emerge from a compact, internally consistent dataset when complete processing histories, rapid performance measurements, and feasibility feedback are preserved. More systematic reporting of successful, partially realized, and unsuccessful processing histories would sub-

stantially increase the value of future materials datasets for this class of problems. [5]

As AI becomes more widely used in materials research, we reiterate that processing should be treated as a design space alongside composition and structure. [5] The objective should not automatically be assumed to collect the largest data set, perform the most characterization, or construct the most accurate predictive model. A more consequential question is what information is required to make the next useful experimental decision, and when additional information becomes worth acquiring. The goal of closed-loop AI should, therefore, not be to characterize everything faster, but to determine what must be measured next to be most productive or informative or cost-effective.

Methods

Material preparation and initial conditions

A lean ZX10 magnesium alloy with a nominal composition of Mg–1Zn–0.3Ca–0.15Mn (wt.%) was used throughout this study. All experiments were conducted at a fixed alloy composition to isolate the effects of processing history on the measured mechanical and corrosion properties. The alloy was cast and homogenized before conventional extrusion at 350 °C using an extrusion ratio of 25:1, producing cylindrical rods approximately 12 mm in diameter. A subset of the extruded material was subsequently subjected to eight passes of continuous equal-channel angular pressing (ECAP) using route B_c, with four passes at 300 °C followed by four passes at 250 °C, following previously established procedures [26, 28, 35]. The grain structures and crystallographic textures of these precursor states have been characterized previously [26, 28].

A solution-treated reference condition was prepared by heating ECAP-processed material at 450 °C for 128 h under flowing Ar, followed by rapid water quenching. The extruded (EXT), ECAP-processed (ECAP), and solution-treated (ST) states provided the three principal material conditions used to construct the initial experimental dataset. Subsequent thermomechanical operations were applied to these precursor states to generate distinct processing histories at constant alloy composition.

Thermomechanical processing procedures

Thermomechanical processing consisted of cold rolling and thermal treatment, applied individually or in sequential combinations. Cold rolling was performed at approximately 25 °C using an International Rolling Mill laboratory rolling mill, following previously established procedures [8, 27]. Thickness reductions were introduced incrementally over multiple passes, typically requiring approximately 10 passes to achieve the prescribed reduction, depending on the processing condition. Specimen thickness was measured before and after rolling to determine the experimentally achieved reduction. Rolling deformation was represented using logarithmic thickness strain and nominal strain rate, with their mathematical definitions and calculation procedures provided in the Supplementary Information (SI 1.1).

Thermal treatments at temperatures up to approximately 250 °C were performed using a Carbolite laboratory oven, with specimens immersed in silicone oil to promote uniform heat transfer and limit direct atmospheric exposure. Higher-temperature treatments were performed under flowing Ar using a Carbolite Gero HTCR5/95 furnace. Treatment temperatures and durations were varied according to the prescribed processing pathways.

Each processing pathway was implemented in its prescribed chronological order. Rolling reductions were attempted as recommended, subject to the experimental deformation limits of the material. When the target reduction could not be achieved without macroscopic cracking or loss of sufficient specimen geometry for subsequent testing, rolling was stopped at the maximum achievable reduction. The actual thickness reduction was recorded, allowing deviations between recommended and experimentally realized pathways to be quantified. All recommended thermal treatments were implemented at their prescribed temperatures and durations.

Processing space and pathway representation

The initial dataset comprised 40 experimentally produced processing states spanning extrusion, ECAP, cold rolling (at 25 °C), solution treatment, thermal treatment, and sequential deformation–thermal pathways. During closed-loop optimization, all candidate pathways began from the ECAP-processed state and contained up to two rolling stages and three thermal-treatment stages. Individual stages could remain inactive, allowing processing pathways of different lengths and operation sequences to be considered within a common candidate space.

Candidate processing histories were described using variables representing deformation strain rate, thermal-treatment temperature and duration, and the stage at which each operation occurred within the thermomechanical sequence. This stage-specific description allowed the framework to distinguish pathways containing similar individual operations positioned differently within the processing history. The initial bounds of the processing variables were informed by prior experimental experience, [26–28] considering deformation limits associated with sample cracking or fracture, thermal-treatment temperatures relative to the alloy's melting point, and treatment durations compatible with industrial processing.

The admissible processing ranges were refined between optimization rounds as experimental information regarding physical feasibility accumulated. The observed deformation limits were used to revise the allowable rolling bounds, while excessively long thermal-treatment durations were removed from subsequent search spaces to improve their practical relevance. Complete processing histories, descriptor definitions, and prescribed-versus-achieved

rolling reductions are provided in the Supplementary Information.

Closed-loop optimization and model refinement

The optimization of thermomechanical processing pathways was performed using the PAL 2.0 framework [32, 33], which combines Bayesian optimization with decision-tree-based feature engineering, neural-network-informed priors, and Gaussian process (GP) surrogate modeling. For the separate-property formulation, two GP surrogate models were employed to predict hardness and corrosion rate, respectively, with prior mean functions $m_1(\mathbf{x}_D)$ and $m_2(\mathbf{x}_D)$ and covariance functions $k_1(\mathbf{x}_D, \mathbf{x}'_D)$ and $k_2(\mathbf{x}_D, \mathbf{x}'_D)$. Here, $\mathbf{x}_D$ denotes the processing descriptors, while the mean and covariance functions characterize the prior distributions of the corresponding property responses. The GP posterior distributions were updated using experimentally measured properties as additional data became available. The underlying surrogate-model architecture, posterior construction, and model-updating procedures have been described previously [32, 33].

The optimization objectives and candidate-selection strategy were modified across the three experimental rounds. In Round 1, processing recommendations were generated by maximizing the hardness-to-corrosion-rate ratio. Beginning in Round 2, hardness and corrosion rate were treated as separate objectives, with the corresponding GP models used to generate recommendations by alternately maximizing hardness and minimizing corrosion rate. This separate-objective formulation was retained in Round 3, with additional restrictions imposed on the processing space.

The admissible processing bounds were progressively refined based on the experimental feasibility assessments described above. Following Round 1, the allowable rolling-strain ranges were reduced to account for experimentally observed deformation limits, while the permitted thermal-treatment durations were shortened. The Round 2 experiments further identified the second rolling stage as the principal remaining deformation constraint, allowing its admissible range to be independently refined. For Round 3, the temperature and duration of the final thermal-treatment stage were constrained to 50–200 °C and 1–12 h, respectively. The rolling strains and the temperatures and durations of the preceding thermal-treatment stages were additionally restricted to within 5% of the hardness-optimal values identified during the earlier rounds.

Prior to Round 3, LASSO regression was performed using the available experimental data to assess the relative contributions of individual processing descriptors to hardness and corrosion rate. The resulting coefficients were examined to identify stage-specific associations with each property. A LASSO-inspired linear prior was also incorporated into the corrosion-rate GP model for the final optimization round to inform its posterior predictions.

Rapid property feedback

Vickers microhardness and 24-h immersion corrosion measurements were used as rapid experimental feedback signals during closed-loop optimization.

Vickers microhardness measurements were performed using a LECO AMH55 hardness tester at a load of 500 gf and a dwell time of 15 s. Specimens were mechanically polished through P4000 SiC paper followed by 0.05 μm colloidal silica to obtain a mirror finish. Ten spatially separated indentations were acquired for each processing condition, with adjacent indents separated by at least six times the mean indentation diagonal in accordance with ISO 6507 [36]. Hardness values were calculated using Cornerstone software and are reported as mean ± standard deviation.

For rapid corrosion screening, five independently prepared specimens were tested for each processing condition. Samples were polished through P4000 SiC paper and immersed individually for 24 h in Earle's Balanced Salt Solution (EBSS; Thermo Fisher Scientific) at 37.1 °C under 5% CO_2. Testing followed ASTM G31 using a solution-volume-to-exposed-surface-area ratio of 0.2 mL mm^{-2} [23, 37]. Given the specimen geometry varied with the preceding deformation history, the immersion volume was normalized to the measured exposed surface area of each specimen.

Following exposure, corrosion products were removed according to ASTM G1, and specimen mass was measured before immersion and after post-exposure cleaning [38]. Corrosion rate was calculated independently for each specimen from mass loss according to

$$CR = \frac{KW}{AT\rho}, \tag{1}$$

where CR is the corrosion rate in mm yr^{-1}, $K = 8.76\times10^4$, W is the mass loss in g, A is the exposed surface area in cm^2, T is the exposure time in h and ρ is the alloy density in g cm^{-3}. Corrosion rates are reported as mean ± standard deviation for $n = 5$. Detailed surface-preparation, immersion, cleaning, pH-monitoring and mass-loss procedures are provided in the Supplementary Methods (SI 2.2).

Targeted microstructural characterization

Detailed microstructural characterization was performed after completion of the closed-loop search and was not used as feedback during optimization. The two Round 3 conditions that overlapped the target hardness–corrosion region within experimental uncertainty, R3-R2 and R3-R3, were selected for subsequent characterization.

Samples were sectioned by wire electrical discharge machining and mechanically polished through P4000 SiC paper followed by 0.05 μm colloidal silica. Electron backscatter diffraction was performed using a TESCAN MIRA 3 GM field-emission scanning electron microscope equipped with an Oxford Instruments EBSD detector and operated

at 20 kV. A step size of 0.3 μm was used for the selected ZX10 states. Grain morphology, grain size, crystallographic texture, intragranular misorientation and geometrically necessary dislocation density were evaluated using AZtec Crystal software.

Scanning-electron-microscopy, backscattered-electron and energy-dispersive X-ray spectroscopy measurements were performed using a JEOL IT700HR InTouchScope equipped with an EDAX EDS system. Backscattered-electron images and compositional maps were used to assess second-phase morphology, spatial distribution, composition and microstructural homogeneity. Second-phase characteristics were evaluated using image-analysis procedures established previously [22, 26].

X-ray diffraction measurements were performed using a Malvern Panalytical Aeris diffractometer. Diffraction patterns were collected over a 2θ range of approximately 20–90° and used to compare phase constitution and relative peak intensities among the selected processing states. Detailed specimen preparation, ion milling, EBSD reconstruction, grain-size analysis, dislocation-density estimation, second-phase analysis, and diffraction parameters are provided in the Supplementary Methods (SI 2.1).

Extended property validation

Mechanical performance following closed-loop optimization was evaluated by micro-tensile testing of R3-R2 and R3-R3 together with the solution-treated reference condition. Micro-tensile specimens were precision-cut by wire electrical discharge machining and had a gauge length of 4 mm, width of 1 mm, and thickness of 1.5 mm, consistent with established procedures based on ASTM B557M [26]. ECAP-derived specimens were extracted at approximately 45° relative to the longitudinal ECAP direction.

Testing was performed using a Kammrath & Weiss micro-tensile stage equipped with a 5 kN load cell at a nominal quasi-static strain rate of approximately 10^{-3} s^{-1}. Surface deformation was recorded by video and analyzed by two-dimensional digital image correlation (DIC) using VIC-2D. DIC-derived axial strain from the specimen gauge region was synchronized with the recorded load to construct engineering stress–strain curves and determine the mechanical properties. Representative fracture surfaces were subsequently examined by SEM. Additional details of tensile data processing and mechanical-property calculations are provided in the Supplementary Methods (SI 2.2).

Longer-duration corrosion testing was performed over 14 days in EBSS, Hank's Balanced Salt Solution and Dulbecco's Modified Eagle Medium without fetal bovine serum. Five independently prepared specimens were tested for each material condition and medium. Experiments were conducted at 37.1 °C under 5% CO_2 using a solution-volume-to-exposed-surface-area ratio of 0.2 mL mm^{-2} in accordance with the same general mass-loss framework used for rapid screening [23, 37]. Solution pH was measured daily and maintained below 8.0 through periodic medium replacement. Following exposure, specimens were cleaned according to ASTM G1, corrosion rates were calculated from mass loss using Equation (1), and post-exposure surfaces were examined by SEM.

Acknowledgements

The authors extend their sincere gratitude to Rich Middlestadt and Stipe Iveljic (Whiting School of Engineering Manufacturing Facilities) for their invaluable assistance with sample preparation and machining. The authors also thank Beril Ulugun, Tram Nguyen, Rida Chowdhury, Jeremy Zheng, and Diana Bershadsky for initial discussions and preliminary investigations.

We also acknowledge the Materials Characterization and Processing Facility, the Hopkins Extreme Materials Institute (HEMI), and the Whiting School of Engineering Manufacturing Facilities at Johns Hopkins University for materials characterization and sample preparation.

Funding

Sreenivas Raguraman and Timothy P. Weihs were partially supported by the National Science Foundation under Grant DMR-2320355. Maitreyee Sharma Priyadarshini and Paulette Clancy were partially supported by the U.S. Department of Energy (DOE), Office of Science, Basic Energy Sciences (BES), under Award DE-SC0022305 (Formulation Engineering of Energy Materials via Multiscale Learning Spirals). Maitreyee Sharma Priyadarshini was also partially supported by her start-up funds at Virginia Tech. Computational resources were provided by the Advanced Research Computing at Hopkins (ARCH) facility, supported by the National Science Foundation under Award OAC-1920103.

Conflicts of Interest

The authors declare no conflicts of interest.

Data and Code Availability

All data supporting the findings of this study are provided in the main text and Supplementary Information. The PAL 2.0 framework employed for closed-loop optimization in this study is openly available at https://github.com/ClancyLab/PAL2.

References

[1] A. Merchant, S. Batzner, S. S. Schoenholz, M. Aykol, G. Cheon, E. D. Cubuk, Scaling deep learning for materials discovery, Nature 624 (7990) (2023) 80–85.

[2] G. L. Hart, T. Mueller, C. Toher, S. Curtarolo, Machine learning for alloys, Nature Reviews Materials 6 (8) (2021) 730–755.

[3] C. Duan, A. Nandy, H. J. Kulik, Machine learning for the discovery, design, and engineering of materials, Annual Review of Chemical and Biomolecular Engineering 13 (1) (2022) 405–429.

[4] J. Fang, M. Xie, X. He, J. Zhang, J. Hu, Y. Chen, Y. Yang, Q. Jin, Machine learning accelerates the materials discovery, Materials Today Communications 33 (2022) 104900.

[5] S. Raguraman, A. Griebel, M. S. Priyadarshini, P. Clancy, T. P. Weihs, A call to elevate the role of processing in ai-driven materials design, Nature Reviews Materials 10 (12) (2025) 875–876.

[6] K. N. Sasidhar, N. H. Siboni, J. R. Mianroodi, M. Rohwerder, J. Neugebauer, D. Raabe, Enhancing corrosion-resistant alloy design through natural language processing and deep learning, Science Advances 9 (32) (2023) eadg7992.

[7] A. K. Cheetham, R. Seshadri, Artificial intelligence driving materials discovery? perspective on the article: Scaling deep learning for materials discovery, Chemistry of Materials 36 (8) (2024) 3490.

[8] A. Kim, S. Raguraman, A. J. Griebel, T. P. Weihs, Enhancing the hardness–corrosion balance in lean mg–ca alloys via post-extrusion thermomechanical processing, in: TMS Annual Meeting & Exhibition, Springer, 2026, pp. 1367–1379.

[9] Y. Yang, S. Hinduja, Sequence planning of sheet metal parts manufactured using progressive dies, The International Journal of Advanced Manufacturing Technology 124 (7) (2023) 2199–2214.

[10] Y. Chen, Y. Tian, Y. Zhou, D. Fang, X. Ding, J. Sun, D. Xue, Machine learning assisted multi-objective optimization for materials processing parameters: a case study in mg alloy, Journal of Alloys and Compounds 844 (2020) 156159.

[11] M. Ghorbani, M. Boley, P. Nakashima, N. Birbilis, A machine learning approach for accelerated design of magnesium alloys. part a: Alloy data and property space, Journal of Magnesium and Alloys 11 (10) (2023) 3620–3633.

[12] J. Su, L. Chen, S. Van Petegem, F. Jiang, Q. Li, J. Luan, S. L. Sing, J. Wang, C. Tan, Additive manufacturing metallurgy guided machine learning design of versatile alloys, Materials Today (2025).

[13] A. Fadhel, N. W. Zuckschwerdt, A. Deshwal, S. Bose, A. Bandyopadhyay, J. Doppa, Ai-driven discovery of feasible 3d printing configurations for metal alloys, AI Magazine 47 (3) (2026) e70069.

[14] G. Lambard, Beyond structure: revolutionising materials discovery via ai-driven synthesis protocol-property relationships, Journal of Physics: Materials 9 (2) (2026) 021003.

[15] A. Molkeri, D. Khatamsaz, R. Couperthwaite, J. James, R. Arróyave, D. Allaire, A. Srivastava, On the importance of microstructure information in materials design: Psp vs pp, Acta Materialia 223 (2022) 117471.

[16] D. Khatamsaz, V. Attari, R. Arroyave, Microstructure-aware bayesian materials design, Acta Materialia (2025) 121587.

[17] T. Hastings, M. Mulukutla, D. Khatamsaz, D. Salas, W. Xu, D. Lewis, N. Person, M. Skokan, B. Miller, J. Paramore, et al., Accelerated multi-objective alloy discovery through efficient bayesian methods: Application to the fcc alloy space, arXiv preprint arXiv:2405.08900 (2024).

[18] S. Lo, S. G. Baird, J. Schrier, B. Blaiszik, N. Carson, I. Foster, A. Aguilar-Granda, S. V. Kalinin, B. Maruyama, M. Politi, et al., Review of low-cost self-driving laboratories in chemistry and materials science: the "frugal twin" concept, Digital Discovery 3 (5) (2024) 842–868.

[19] Z. Pei, K. A. Rozman, Ö. N. Doğan, Y. Wen, N. Gao, E. A. Holm, J. A. Hawk, D. E. Alman, M. C. Gao, Machine-learning microstructure for inverse material design, Advanced Science 8 (23) (2021) 2101207.

[20] M. K. Miller, T. F. Kelly, K. Rajan, S. P. Ringer, The future of atom probe tomography, Materials Today 15 (4) (2012) 158–165.

[21] Y. F. Zheng, X. N. Gu, F. Witte, Biodegradable metals, Materials Science and Engineering: R: Reports 77 (2014) 1–34.

[22] S. Raguraman, M. L. Connon, C. N. Byrum, R. Berlia, V. Ivanovskaya, B. Ulugun, S. E. Prameela, R. J. Guillory II, T. P. Weihs, Microstructure regulates early-stage corrosion behavior and systemic aluminum fate in biodegradable mg–al alloys: Integrated in-vitro and in-vivo insights, Acta Biomaterialia 208 (2025) 565–580.

[23] S. Raguraman, B. Ulugun, T. Ayodeji, R. Chowdhury, A. Griebel, T. Weihs, Evaluating In-Vitro Corrosion Testing of ECAP-Processed Lean Magnesium Alloys: The Critical Role of Degradation Media Composition, Buffering, and Volume, JOM (Feb. 2025). doi:10.1007/s11837-025-07176-7.

[24] S. Prasadh, S. Raguraman, R. Wong, M. Gupta, Current status and outlook of temporary implants (magnesium/zinc) in cardiovascular applications, Metals 12 (6) (2022) 999.

[25] S. Prasadh, S. Raguraman, R. Wong, M. Gupta, Metallic foams in bone tissue engineering, in: Nanoscale Engineering of Biomaterials: Properties and Applications, Springer, 2022, pp. 181–205.

[26] S. Raguraman, A. Kim, T. Ayodeji, A. J. Griebel, D. Bershadsky, T. Nguyen, T. P. Weihs, Simultaneous Optimization of Strength and Bio-Corrosion Resistance in Biodegradable ZX10 Magnesium Alloy via Thermomechanical Processing and Annealing, Journal of Alloys and Compounds (2025) 180078.

[27] S. Raguraman, R. McGovern, A. Kim, V. Ivanovskaya, T. Nguyen, T. Ayodeji, A. Griebel, T. Weihs, Impact of Thermo-Mechanical Processing on Structure–Property Relationships for the Biodegradable ZX10 Mg alloy, in: A. Leonard, S. Barela, N. R. Neelameggham, V. M. Miller, D. Tolnai (Eds.), Magnesium Technology 2024, Springer Nature Switzerland, pp. 213–216. doi:10.1007/978-3-031-50240-8_40.

[28] S. Raguraman, M. S. Priyadarshini, T. Nguyen, R. McGovern, A. Kim, A. J. Griebel, P. Clancy, T. P. Weihs, Machine learning-guided accelerated discovery of structure-property correlations in lean magnesium alloys for biomedical applications, Journal of Magnesium and Alloys (Jun. 2024). doi:10.1016/j.jma.2024.06.008.

[29] Z. Shi, M. Liu, A. Atrens, Measurement of the corrosion rate of magnesium alloys using tafel extrapolation, Corrosion science 52 (2) (2010) 579–588.

[30] M. Esmaily, J. Svensson, S. Fajardo, N. Birbilis, G. S. Frankel, S. Virtanen, R. Arrabal, S. Thomas, L. Johansson, Fundamentals and advances in magnesium alloy corrosion, Progress in Materials Science 89 (2017) 92–193.

[31] P. Zhang, S. Li, Z. Zhang, General relationship between strength and hardness, Materials Science and Engineering: A 529 (2011) 62–73.

[32] M. S. Priyadarshini, O. Romiluyi, Y. Wang, K. Miskin, C. Ganley, P. Clancy, Pal 2.0: a physics-driven bayesian optimization framework for material discovery, Materials Horizons 11 (3) (2024).

[33] M. Sharma Priyadarshini, E. Gienger, J. Ren, B. Piloseno, E. A. Pogue, P. K. Lambert, J. S. Ko, P. Clancy, Machine learning-driven closed-loop discovery of hard multiple principal element alloys, Materials Horizons 13 (18) (2026) 9152–9163.

[34] A. Bahmani, S. Arthanari, K. S. Shin, Formulation of corrosion rate of magnesium alloys using microstructural parameters, Journal of Magnesium and Alloys 8 (1) (2020) 134–149. doi:10.1016/j.jma.2019.12.001.

[35] C. F. Davis, A. J. Griebel, T. C. Lowe, Isothermal Continuous Equal Channel Angular Pressing of Magnesium Alloy AZ31, JOM 72 (7) (2020) 2603–2611. doi:10.1007/s11837-020-04195-4.

[36] International Organization for Standardization, ISO 6507-1:2023(en), Metallic materials — Vickers hardness test — Part 1: Test method.
URL https://www.iso.org/obp/ui/#iso:std:iso:6507:-1:ed-5:v1:en

[37] J01 Committee, Guide for Laboratory Immersion Corrosion Testing of Metals, Tech. rep., ASTM International. doi:10.1520/G0031-72R04.
URL http://www.astm.org/cgi-bin/resolver.cgi?G31-72R04

[38] G01 Committee, Practice for Preparing, Cleaning, and Evaluating Corrosion Test Specimens. doi:10.1520/G0001-03R17E01.
URL http://www.astm.org/cgi-bin/resolver.cgi?G1-03R17E1

Supplementary Files

This is a list of supplementary files associated with this preprint. Click to download.

- ClosedLoopMLZX10MagnesiumSI.pdf